Journal of Advanced Ceramics
2023, **12**(8): 1612–1624
https://doi.org/10.26599/JAC.2023.9220775
ISSN 2226-4108
CN 10-1154/TQ

Research Article

A creative method to tune Fe–O interaction in ferrites

Farshad Farshidfar[a], Arash Fattahi[a], Ralf Brüning[b], Dominic H. Ryan[c], Khashayar Ghandi[a,*]

[a]*Department of Chemistry*, *University of Guelph*, *Guelph N1G 2W1*, *Canada*
[b]*Physics Department*, *Mount Allison University*, *Sackville E4L 1E6*, *Canada*
[c]*Physics Department*, *McGill University*, *Montreal H3A 2T8*, *Canada*

Received: February 1, 2023; Revised: May 21, 2023; Accepted: May 30, 2023

Abstract: To be able to regulate the anionic oxygen position in ferrites, an original compositing method is developed by introducing a porous p-type phase in the n-type matrix of ferrite spinel semiconductors. A result of this method is the synergetic effect of the enhanced mass and charge transport that impacted the morphology and anionic oxygen position within the $MgFe_2O_4$ structure. Our hypothesis is that fine tuning of the anionic oxygen position in ferrites allows us to regulate their physicochemical properties significantly, with the implications for diverse applications. The electron exchange interaction (J) between O-centered and octahedral-occupying iron (Fe)-centered orbitals affected both the electrical and magnetic properties of the matrix significantly, supporting our hypothesis. The three-dimensional variable range electron hopping is one such effect.

Keywords: $MgFe_2O_4$; spinel; structural distortion; electron hopping

1 Introduction

Spinels are formed in natural reserves [1,2], and have been developed in the laboratories for a diverse range of applications [3–12]. Although challenging, understanding the mechanism of electron transport in both monophase and multiphase semiconductor spinels is important for the applications such as sensors reported recently for the $MgFe_2O_4$–Mn_3O_4 composite [13] and for biomedical applications [14,15]. Developing such an understanding of ferrite spinels, such as $MgFe_2O_4$, is the purpose of this study. Our hypothesis is that by fine tuning of anionic oxygen position in ferrites, their properties would be controlled significantly. We developed a novel compositing method to allow us to develop such fine control of anionic oxygen position aiming at the enhanced mass and charge transport.

$MgFe_2O_4$ is known as a typically mixed ferrite spinel with the structural formula of $(Mg_{1-\alpha}Fe_{\alpha})[Mg_{\alpha}Fe_{2-\alpha}]O_4$, where ( ) and [ ] represent the tetrahedral and octahedral sites, respectively, and α represents the degree of inversion describing cation distribution [16–22]. α ranges from 0 for the normal $(Mg)[Fe_2]O_4$ structure to 1 for the inversed $(Fe)[Mg,Fe]O_4$ structure. Any value in this range is considered as a mixed cation distribution [23].

Magnesium cation (Mg^{2+}) is an inactive component of $MgFe_2O_4$ electrically and magnetically, which is why it is selected to reduce the number of the parameters affecting the physical properties. A stoichiometric magnesium ferrite spinel with the average iron (Fe) valance state of +3 is an electrically insulator [24–26].

* Corresponding author.
E-mail: kghandi@uoguelph.ca

Enhanced electrical conductivity (σ) and electrocatalytic activity of spinel ferrites via oxygen deficiency (x and x'), also called vacant or defected oxygen, have been reported through harsh chemical treatment at low temperatures (T) or thermal treatment in a reductive environment at temperatures typically above 500 ℃ [27–31]. Removing molecular oxygen from AB_2O_4 spinels, where A and B are denoted as +2 and +3 cations, respectively, is accompanied by the formation of defective sites (Reaction (1)):

$$AB_2O_4 \rightarrow 2O_2 + A_i^{\bullet\bullet} + 2B_i^{\bullet\bullet\bullet} + 8e^- \quad (1)$$

where dots are designated as the oxidation state, and i is the interstitial defect site. The electrons depicted in Reaction (1) can reduce the interstitial cations, as previously observed in $NiFe_2O_4$ and $CuFe_2O_4$ [32,33]. In this work, we study the effects of defects and distortions on charge carrier transport through the ferrite spinel structure. For this purpose, a novel semiconductor compositing method is developed.

2 Method

The co-precipitation method was used to form the $MgFe_2O_4$ spinel [34]. The details are described in Figs. S1–S3 in the Electronic Supplementary Material (ESM) and briefly outlined here. $Mg(NO_3)_2{\cdot}6H_2O$ (Sigma-Aldrich, ACS reagent, 99%) and $Fe(NO_3)_3{\cdot}9H_2O$ (Sigma-Aldrich, ACS reagent, > 98%) were added to deionized water to form a slurry. NaOH (Sigma-Aldrich, > 98%), dissolved in deionized water, was added dropwise to the well-stirred slurry to adjust the pH to 9 at 60 ℃. After repeated filtration to wash away the remaining sodium, the precipitate was dried at 110 ℃. To prepare the $Mn_3O_4/MgFe_2O_4$ composite containing 10 mol% of Mn_3O_4, an appropriate amount of MnO_2 (Sigma-Aldrich, 10 μm, ⩾ 90%) was dry mixed thoroughly with the finely powdered prepared precipitate. The powders were pressed to pellets with 15 mm in diameter and 2 mm in thickness followed by heating in a quartz tube at 850 ℃ for 3 h under an ultra-high purity nitrogen to form the spinel structure with a dispersed Mn_3O_4 phase. These conditions were selected based on the known phase diagram of Mn–O, which shows that Mn_3O_4 is the most stable phase at 850 ℃ under nitrogen or low partial pressures of oxygen [35–37].

The scanning electron microscopy (SEM) images were taken using FEI Quanta FEG 250 equipped with an InLens detector (Zeiss, Germany). The room-temperature Mössbauer spectra were collected on a conventional constant-acceleration spectrometer (Wissenschaftliche Elektronik GmbH, Germany) that was calibrated using a thin iron–metal foil. A velocity of zero was set as the centroid of the calibration spectrum. The samples were hand ground to fine powders and mixed with boron nitride to make a uniform absorber.

A custom-built θ–θ diffractometer equipped with pyrolytic graphite monochromator and analyzer crystals (grade ZYA, Advanced Ceramics, Ohio) was utilized to carry out the X-ray diffraction (XRD) measurements with the Cu-Kα radiation at the wavelength of 0.15406 nm. Background scattering was avoided by placing samples on a Si 511 crystal. The evacuation of the sample environment avoided air scattering. The Rietveld refinement of the XRD patterns were done by Materials Analysis Using Diffraction (MAUD) software (version 2.992 written in Java by Luca Lutterotti, Italy), and the least-square parameter (R_{wp}) was used to evaluate the refinement. Both the Williamson–Hall and Scherrer methods are utilized to evaluate the crystallite size [38].

The Fourier transform infrared (FTIR) spectra were collected from 400 to 4000 cm^{-1} by an FITR spectrometer (ALPHA II, Bruker, Germany). A correlation between the Rietveld-refined XRD pattern and FTIR spectra allowed us to establish the structural details. The oxidation kinetics was studied via our in-house developed instrument (Fig. 1) to measure the electrical conductivity *in situ*. A custom-built setup

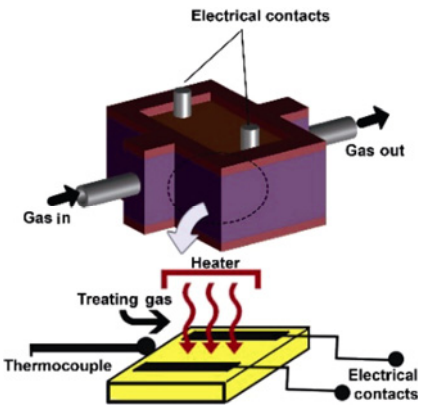

Fig. 1 Sealed conductivity measurement cell equipped with gas inlet and outlet (top) and pellet adjacent to heater and thermocouple (down) for measuring electrical properties.

with the gas–solid interface and an *in situ* surface conductivity probe (Fig. S2 in the ESM) were utilized for this purpose. The polished square-shaped pellets were reduced in ultra-high purity grade nitrogen at 250 ℃ for two weeks prior to evaluating the oxidation kinetics.

The X-ray photoelectron spectroscopy (XPS; Figs. S6–S8 in the ESM) measurements are done under ultra-vacuum by an X-ray photoelectron spectrometer (Argus CU, Scienta Omicron) using a monochromatic Al Kα source (16 mA, 12 kV). The survey scans with a pass energy of 200 eV were deconvoluted by CasaXPS software (Casa Software version 2.3.24PR1.0 Ltd., UK). The magnetic susceptibility (χ) in emu/(g·Oe) was collected via the physical property measurement system (PPMS; Quantum Design, USA).

3 Results and discussion

The SEM images are shown in Figs. 2(a)–2(c). The SEM images of the $Mn_3O_4/MgFe_2O_4$ composite confirm the formation of the isolated porous Mn_3O_4 particles dispersed in a matrix of the $MgFe_2O_4$ spinel (Fig. 2(a)). During calcination, MnO_2 is first reduced to Mn_2O_3, and then further to Mn_3O_4. These reduction steps are consistent with the observations for pure MnO_2 by Terayama and Ikeda [37]. There are two types of pores that can be seen in Fig. 2. Some are the pores between particles (interparticle pores) and some are within the particles (intraparticle pores). The intraparticle pores in the Mn_3O_4 phase with pore dimeters in the range of 5–10 μm (Fig. 2(c)) are obvious. Their formation is assumed to be due to the releasing oxygen in the calcination process based on our designed synthetic process. Such intraparticle pores were not observed in the bare $MgFe_2O_4$ particles (Fig. S4 in the ESM).

The Mössbauer spectra (Fig. 3) consisted of broadened magnetic patterns which are likely the results of disordered and random iron distributions between the tetrahedral and octahedral sites, respectively. The similarity of both patterns confirms that the inversion degree of $MgFe_2O_4$ was not affected by introducing Mn_3O_4 as a secondary phase. We found that a simple sum of sharp magnetic sextets would not yield satisfactory fits, so we used sextets that were convoluted with an asymmetric Gaussian distribution of hyperfine fields (broader on the low-field side of the distribution, as is typical of disordered systems). Typical peak fields were in the range of 45–48T, with widths of about 1T (high side) and 3T (low side). As many as four broadened sextets were needed to provide adequate fits, however, as none of them was clearly resolved, we hesitate to attribute any fitting component to a specific feature of a material. Hence, complementary methods such as the XPS, XRD, and magnetic measurements were applied.

The volume fraction of the Mn_3O_4 phase is 5.7%±0.1% based on the refined XRD patterns (Fig. 4), consistent with the 7.4% area obtained by the SEM–EDX data (Fig. 2(a)). This further supports that there is negligible diffusion of Mn in $MgFe_2O_4$. The volume shrinkage, water absorption, and porosity are

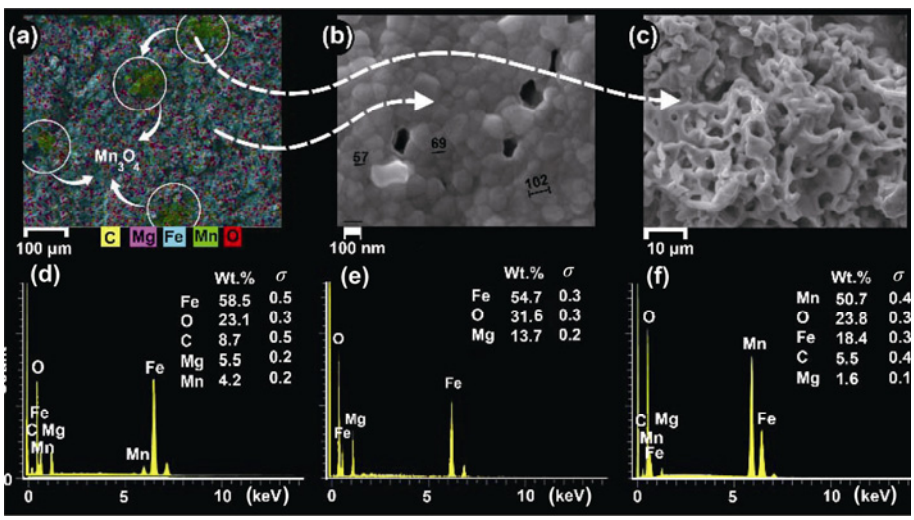

Fig. 2 (a) Energy dispersive X-ray (EDX) spectral mapping and SEM image of $Mn_3O_4/MgFe_2O_4$ composite; high-resolution SEM images of (b) $MgFe_2O_4$ matrix and (c) Mn_3O_4 phase with intraparticle pores; and (d–f) corresponding EDX quantitative analysis.

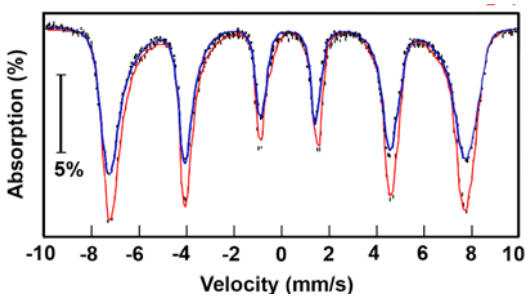

Fig. 3 Mössbauer spectra of bare $MgFe_2O_4$ (red) and $Mn_3O_4/MgFe_2O_4$ composite (blue).

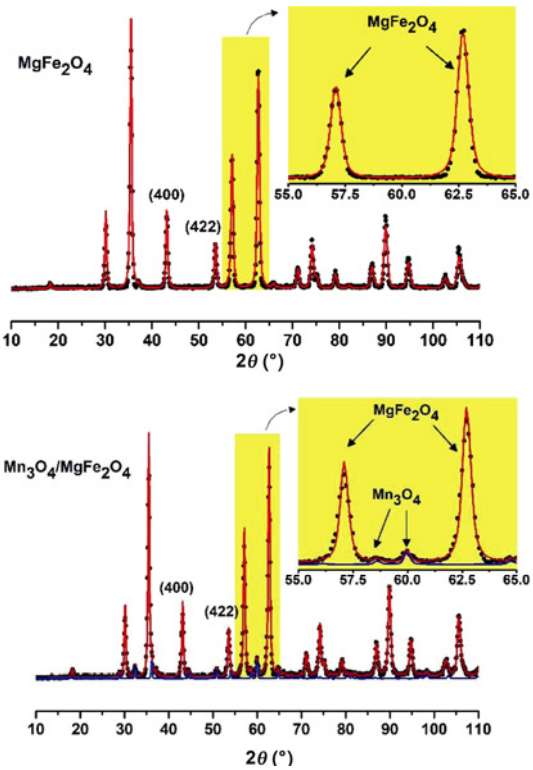

Fig. 4 Rietveld-refined XRD patterns of bare $MgFe_2O_4$ and $Mn_3O_4/MgFe_2O_4$ composite.

calculated (Eqs. (S1)–(S3) in the ESM) and reported (Table S1 in the ESM). The introduction of Mn_3O_4 increased the porosity by almost 5% in the form of intraparticle pores based on the observed density and X-ray density extracted from the XRD.

The calcination temperature of 850 ℃ under a nitrogen environment was the best condition to obtain the nanoscale crystallites with negligible solid solution. A nanocrystalline texture with the sizes of 13.76±0.67 and 12.09±0.94 nm was obtained for bare $MgFe_2O_4$ and $Mn_3O_4/MgFe_2O_4$ composite, respectively. These values are extracted based on the Williamson–Hall equation (Fig. S9 in the ESM). These values are about 1/6 of the average particle size (77 nm) from the SEM images. This observation confirms the nature of polycrystallinity. The negative slope (~−0.002) of the plot $\beta_{hkl}\cos\theta$ vs. $4\sin\theta$ (Fig. S9 in the ESM) indicates that the negative strain generated most probably due to oxygen deficiency. Based on the Scherer method and using the full width at half maximum (FWHM) values of the (311) peak (Fig. S3 in the ESM), the crystallite size doubles in air at 850 ℃ and increases by 5-fold at 1300 ℃ while getting Mn dissolved in the $MgFe_2O_4$ matrix. The absence of Fe_2O_3 as a secondary phase supports a high rate of spinel formation at 850 ℃ under nitrogen. This is most probably due to the increasing oxygen vacancy concentration and cationic diffusion rate [39].

The lattice constant of $MgFe_2O_4$ is 8.383(1) Å (standard range: 8.38–8.40 Å [9,40,41]), denoting the high α [42,43]. This is also confirmed by the calculated α value of 0.83 referring to the peak ratio of I_{400}/I_{422} being ~1.6 based on the Bertaute method for $MgFe_2O_4$ [44]. Introducing Mn_3O_4 as the secondary phase did not alter the lattice constant, the crystallite size, and the cation distribution, confirming negligible solid solution for the materials that is formed at 850 ℃ under nitrogen and suggesting the minimized Jahn–Teller distortion effect of Mn cation on the symmetric cubic structure of $MgFe_2O_4$. In such a binary phase composite, the dissimilarity of Mn_3O_4 and $MgFe_2O_4$ in tetragonal and cubic symmetry settings, respectively, makes the refined parameters recognizable from each other. The lattice parameters of Mn_3O_4 fraction are $a = b = 5.762(1)$ Å and $c = 9.486(1)$ Å, and the lattice parameters of $MgFe_2O_4$ phase are $a = b = c = 8.383(1)$ Å.

Following Ref. [45], we employed the generalized anion position parameter (u) to define the oxygen position in the structure, which is 0.2500 for an ideal *Fd3m* structure (Eqs. (S4) and (S5) in the ESM) [46]. Based on the Rietveld refinement parameters (Table 1), the [Fe]–O distance in the bare $MgFe_2O_4$ is less than that in the $Mn_3O_4/MgFe_2O_4$ composite. This is due to the displacement of the anionic oxygen by approximately 1% of its radius (126 pm) in the bare $MgFe_2O_4$. This seemingly slight change shifts the electron density from the oxygen anion to iron cation significantly [20]. Hence, the anion–cation interaction at the octahedral site in a $Mn_3O_4/MgFe_2O_4$ composite is expected to be smaller than that for bare $MgFe_2O_4$. Therefore, the only physicochemical effect of introducing Mn_3O_4 on $MgFe_2O_4$ (other than intraparticle pores) is

the slight shift of anionic oxygen away from cation. The shift in the position of oxygen affects the electron transport via the electron exchange interaction (J) between two adjacent iron cations. This phenomenon occurs between the two adjacent orbitals of Fe^{2+} and Fe^{3+} either occupying edge sharing octahedral sites shown as [Fe]–O–[Fe] or corner sharing octahedral and tetrahedral sites shown as [Fe]–O–(Fe). The two oxygen sharing sites and the electronic configurations associated with the electron transport are illustrated in Fig. 5. Due to a shorter hopping length and the higher abundancy of the octahedral sites, the electron hopping occurs most probably between iron cations occupying octahedral sites. The electron exchange interaction via (Fe)–O–(Fe) is unlikely to happen because of the long hopping length and the missing shared oxygen.

Table 1 Rietveld refinement parameters of $MgFe_2O_4$ phase based on the XRD patterns

	$MgFe_2O_4$	$Mn_3O_4/MgFe_2O_4$
α	0.83	0.83
R_{wp}	0.24	0.17
R_p	0.17	0.11
Lattice constant (Å)	8.383(1)	8.383(1)
(Fe)–(Fe) bond length (Å)	3.629(1)	3.628(1)
[Fe]–[Fe] bond length (Å)	2.963(1)	2.963(1)
(Fe)–[Fe] bond length (Å)	3.473(2)	3.474(2)
(Fe)–O bond length (Å)	1.979(1)	1.885(1)
[Fe]–O bond length (Å)	2.005(1)	2.056(2)
U	0.2613(1)	0.2548(1)

Note: R_p: residual of least-square refinement; R_{wp}: weighted residual of least-square refinement.

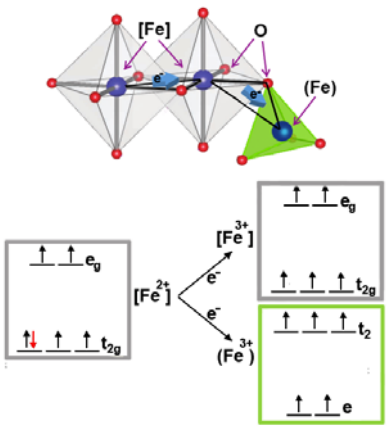

Fig. 5 (a) Iron at octahedral sites [Fe] and tetrahedral site (Fe) with edge and corner sharing oxygen, respectively; (b) electron hopping from [Fe^{2+}] to either adjacent [Fe^{3+}] or (Fe^{3+}), where the excess electron in $3d^6$ orbital contributing to the electron transfer is shown in the red colour.

The FTIR spectra (Fig. 6) further supports our conclusion about the change in the position of oxygen. The absence of stretching vibrations of nitrate, hydroxide, and carbonate species and the appearance of two absorption bands in the range of 400–600 cm^{-1} confirm the complete decomposition of precursors to the spinel structure. The bands at higher and lower wavenumbers are attributed to the oxygen–cation bonds in the tetrahedral and octahedral sites, respectively. The absorption band shifts to higher wavenumbers by decreasing the cation–anion distance, therefore increasing the force constants [47,48] of bonds at the octahedral (K_O) and tetrahedral sites (K_T) (Eqs. (S6)–(S8) in the ESM). Accordingly, the observed band shift of the tetrahedral vibration mode from 543 to 562 cm^{-1} corresponds to the change of the force constant from 210.83 to 225.84 $N \cdot m^{-1}$. A smaller force constant at the tetrahedral sites supports the oxygen shift from the tetrahedral site toward the octahedral site.

The pre-reduced samples under nitrogen at 250 ℃ for two weeks were oxidized through exposure to a continuous ultra-pure grade air flow of 20 mL/min at 250 ℃ while monitoring the electrical conductivity. The σ as a function of time (t) during oxidization by purified air decreases exponentially (Fig. 7).

As the reduced forms of materials get oxidized with purified air at 250 ℃, the electrical conductivity is reduced due to trapping quasi-free electrons by oxygen chemisorption, the behavior of which is consistent with what we expect from an n-type semiconductor [39,49], confirming the dominant role of the $MgFe_2O_4$ matrix of the composite. The oxidation curve of bare $MgFe_2O_4$

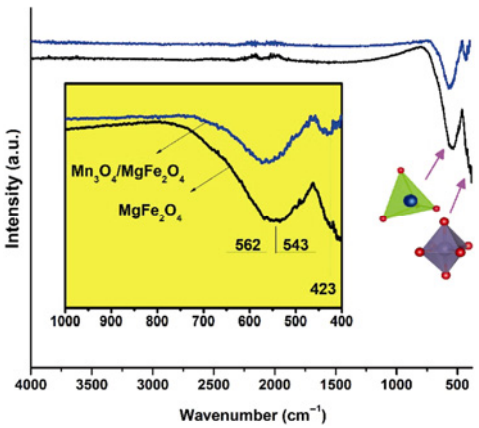

Fig. 6 FTIR spectra of bare $MgFe_2O_4$ and $Mn_3O_4/MgFe_2O_4$ composite with Fe–O vibration bands at tetrahedral and octahedral sites.

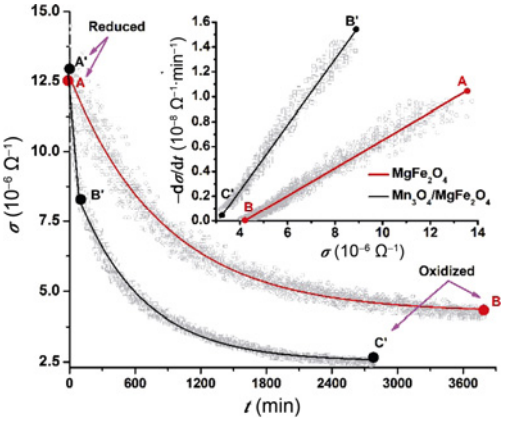

Fig. 7 *In situ* change in surface direct current (DC) σ due to oxidation of bare $MgFe_2O_4$ and $Mn_3O_4/MgFe_2O_4$ composite as a function of time and rate of change of surface electrical conductivity ($-d\sigma/dt$) as a function of σ while being treated with ultra-pure air at 250 ℃.

from point A to point B (Fig. 7) fits simple exponential first-order reaction with respect to the change of the charge density with a rate constant of $1.867(7)\times10^{-5}$ s^{-1} due to oxygen chemisorption. The two-stage oxidation curve of the $Mn_3O_4/MgFe_2O_4$ composite fits a biexponential curve with a fast reaction between A′ and B′ followed by a slow reaction between B′ and C′ with a rate constant of $4.417(2)\times10^{-5}$ s^{-1}. The time resolution required to measure the rate constant of the fast stage is beyond the accuracy of our instrument, but we can provide the lower limit of the rate constant in the fast stage (10^{-2} s^{-1}). Such a fast reaction is remarkable when compared to the other rate constants we reported above for A to B and B′ and C′.

The electron transfer to the chemisorbed oxygen can occur in any form of O_2^-, O^-, or O_2 depending on the temperature. Based on Ref. [29] on other metal oxides, in the temperature range of 150–250 ℃, dissociative adsorption of O_2 (Reaction (4)) is the most favorable mechanism (Reactions (2)–(4)).

$$O_2(\text{gas}) \rightarrow O_2(\text{ads.}) \quad (2)$$

$$O_2(\text{ads.}) + e^- \rightarrow O_2^-(\text{ads.}) \quad T < 100\ ℃ \quad (3)$$

$$O_2(\text{ads.}) + 2e^- \rightarrow 2O^-(\text{ads.}) \quad 100\ ℃ < T < 300\ ℃ \quad (4)$$

The adsorbed oxygen species thicken the electron depletion layer via trapping electrons, which increases the electrical resistance. The oxygen dissociative adsorption step is the rate limiting step for two reasons. One reason is the lower oxygen concentration (in the order of 10^{18} oxygen molecules/cm^3) compared to the electron concentration in a reduced $MgFe_2O_4$ (in the order of 10^{21}–10^{22} electrons/cm^3) [25]. The other reason is the higher energy barrier of the electron transport between the solid and the gas compared to the energy barrier of electron transport in the solid.

The extremely faster oxidation rates by incorporating Mn_3O_4 are due to the enhanced solid–gas interaction at the p-type intraparticle pores and the formation of the p–n heterojunction at the interface of the p-type Mn_3O_4 phase and the n-type $MgFe_2O_4$ matrix. When both come into electrical contact, the Fermi level (E_F) will get into equilibrium by the electron transfer from the n-type side to the p-type side, resulting in charge carrier separation (Fig. 8). High energy electrons accumulated in the p-type side are more reactive to reduce the adsorbed oxygens, which are transported quickly via the intraparticle pores of Mn_3O_4. This is observed in the form of an abrupt drop in the electrical conductivity within the first 80 s of the oxidation process (A′–B′ in Fig. 7). Such an abrupt change is not observed in bare $MgFe_2O_4$. This behavior supports the application of the $Mn_3O_4/MgFe_2O_4$ heterojunction as a sensor.

The surface σ of the reduced and oxidized composites (Fig. 9) increased exponentially with the temperature, consistent with a metal-oxide semiconductor behavior.

The electron hopping activation energy (E_a; Eq. (S9) in the ESM) of the reduced $MgFe_2O_4$ was increased from 0.286(2) to 0.389(2) eV, and the electron hopping activation energy of the reduced $Mn_3O_4/MgFe_2O_4$ composite was increased from 0.303(2) to 0.332(3) eV when oxidized (Tables 2 and 3). The electron hopping energy barrier of bare and composited $MgFe_2O_4$ reported in the current paper is in agreement with the previously reported range of 0.3–0.4 eV for $MgFe_2O_4$

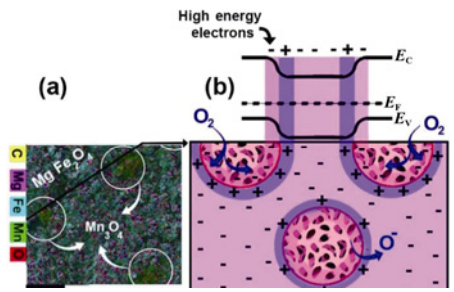

Fig. 8 (a) Cross-section of SEM–EDX mapping of $Mn_3O_4/MgFe_2O_4$ composite, showing intraparticle pores of Mn_3O_4 phase; (b) an illustration of oxygen dissociative adsorption over porous p–n heterojunction interface and formation of anionic oxygen, depicting the electron depletion layer thickening mechanism. Note: E_c is the conduction edge, and E_v is the valance edge.

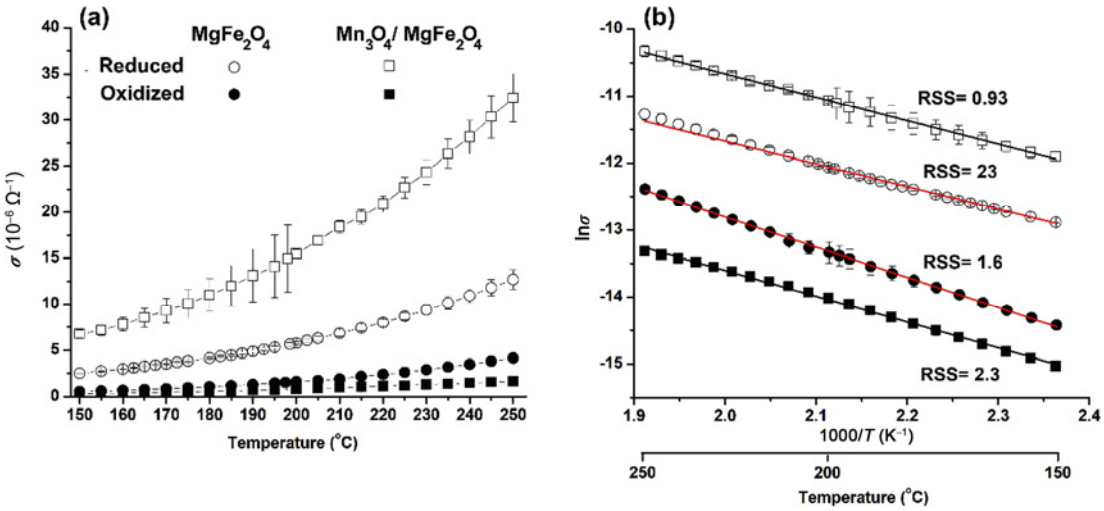

Fig. 9 (a) Surface DC σ of bare $MgFe_2O_4$ and $Mn_3O_4/MgFe_2O_4$ composite as a function of temperature and (b) corresponding lnσ as a function of 1000/T. The lines are the fits to the experimental data. Note: RSS is the abbreviation of weighted residual sum of squares for linear fits.

Table 2 Comparing electron hopping energy barrier for spinels under investigation

Spinel	Electron hopping range (eV)	Ref.
$MgFe_2O_4$	0.29–0.40	This work
$Mn_3O_4/MgFe_2O_4$	0.30–0.33	This work
XFe_2O_4	0.04–0.20	[51–55,59]
Mn_3O_4	0.46–0.74	[56–58]

X = Fe^{2+}, Co^{2+}, Ni^{2+}, Zn^{2+}, and Cu^{2+}.

(Table 2) [50]. This range is higher than the energy barrier of 0.12±0.08 eV across XFe_2O_4, where X is a transition metal cation (Fe^{2+}, Co^{2+},Ni^{2+}, Zn^{2+}, or Cu^{2+}) and less than 0.60±0.14 eV for Mn_3O_4 (Table 2) [51–58]. This confirms that the Mg^{2+} at the octahedral site is increasing the energy barrier, and the dispersed Mn_3O_4 is a non-active phase of the $Mn_3O_4/MgFe_2O_4$ composite in terms of electron hopping with negligible effect on electron transport through the $MgFe_2O_4$ matrix.

Electron hopping occurs via adjacent iron cations, and the significant change in its activation energy is most probably due to the significant shift of the iron oxidation state as the only important component of the ferrite spinel for electron transport across the matrix.

To understand the temperature dependency of electron hopping activation energy over the temperature range of 150–250 ℃, the thermal excitation [60] and three-dimensional variable range hopping models [61] were applied, as illustrated in Fig. 10. The larger values of the weighted RSS of the linear fit of $\ln\sigma$ vs. $1/T$ in the reduced $MgFe_2O_4$ pellet suggest nonlinearity (Fig. 10). However, a significant decrease in the RSS factor of the linear fit of $\ln\sigma$ as a function of $1/T^{1/4}$ supports the three-dimensional variable-range hopping as the dominant mechanism (Fig. 10). Such a deviation from constant electron hopping activation energy in the case of the reduced $MgFe_2O_4$ is eliminated when it is oxidized. Introducing porous Mn_3O_4 particles removed this behavior as well. Such a significant variation in the magnitude of the electron hopping rate and the mechanism of hopping between cations of the spinel structure at the temperature range of 150–250 ℃ is not due to cation rearrangement since the α and hopping length stay constant at this range of temperature [62].

The XPS data were used to further shed light on the changes in the electrical conductivity in the reduced and oxidized forms in the context of changes in the

Table 3 Values of E_a and average valances of iron, manganese, and oxygen

Pellet	Reduced					Oxidized				
	E_a (eV)	RSS	Fe^a	O^a	Mn^a	E_a (eV)	RSS	Fe^a	O^a	Mn^a
$MgFe_2O_4$	0.286(2)	23	+2.4	−1.4	—	0.389(2)	1.6	+2.6	−1.7	—
$Mn_3O_4/MgFe_2O_4$	0.303(2)	0.93	+2.6	−1.5	+2.5	0.332(3)	2.3	+2.7	−1.7	+2.6

[a]average valence.

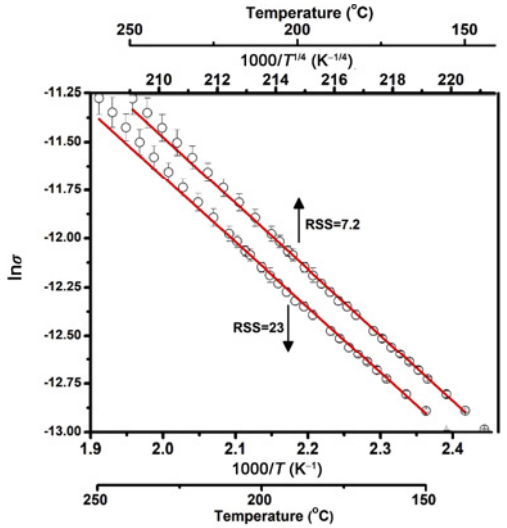

Fig. 10 Linear fits of lnσ vs. 1000/T (the dashed lines) and 1000/$T^{1/4}$ (the solid lines); the error bars are smaller than the symbol size at some temperatures.

oxidation state. The XPS data analysis is illustrated in Section S4 in the ESM. Based on the XPS and XRD evaluations and according to high octahedral occupation preference of Fe^{2+}, as clarified by the crystal field theory, the monophase bare magnesium ferrite spinel can be represented as $(Mg_{0.17}Fe^{3+}_{0.83})[Mg_{0.83}Fe^{3+}_{0.01}Fe^{2+}_{1.16}]O_{4-x}$ and $(Mg_{0.17}Fe^{3+}_{0.83})[Mg_{0.83}Fe^{3+}_{0.39}Fe^{2+}_{0.78}]O_{4-x'}$ in the reduced and oxidized $MgFe_2O_4$, respectively, as shown in the A and B points in Fig. 7, respectively. This indicates that 99% of Fe cations at octahedral sites were reduced. However, by introducing Mn_3O_4, 74% of Fe cations at the octahedral sites of $(Mg_{0.17}Fe^{3+}_{0.83})[Mg_{0.83}Fe^{3+}_{0.51}Fe^{2+}_{0.66}]O_{4-x}$ were reduced to form $(Mg_{0.17}Fe^{3+}_{0.83})[Mg_{0.83}Fe^{3+}_{0.35}Fe^{2+}_{0.82}]O_{4-x}$ due to the diminished [Fe]–O electron exchange interaction. Higher oxygen mobility by introducing intraparticle pores of the Mn_3O_4 phase results in a more homogeneously distributed anionic oxygen vacancies, hence reducing structural distortion as well as Fe–O exchange interaction.

The ratio of the concentration of the oxygen defects in the reduced and oxidized $MgFe_2O_4$ can be estimated as

$$\frac{x}{x'} = [O^-]_{\text{reduced}} / [O^-]_{\text{oxidized}} = \frac{(I_{O^-} / I_{O^{2-}})_{\text{reduced}}}{(I_{O^-} / I_{O^{2-}})_{\text{oxidized}}} \frac{[O^{2-}]_{\text{reduced}}}{[O^{2-}]_{\text{oxidized}}} \approx \frac{(I_{O^-} / I_{O^{2-}})_{\text{reduced}}}{(I_{O^-} / I_{O^{2-}})_{\text{oxidized}}} \quad (5)$$

where $[O^-]$ and $[O^{2-}]$ are the concentrations of oxygen defects and lattice oxygen, respectively, and I_{O^-} and $I_{O^{2-}}$ are the corresponding areas under the XPS peaks (Fig. S8 in the ESM) [63]. Equation (5) is simplified since the variation of the lattice oxygen concentration by reduction and oxidation is negligible. The ratio of electrical conductivity of the reduced and oxidized magnesium ferrite ($\sigma_{\text{reduced}}/\sigma_{\text{oxidized}} = (12.7\times10^{-6})/(4.42\times10^{-6}) = 2.87$) is in good agreement with the value calculated by Eq. (5), confirming that the electrical conductivity is proportional to the oxygen defect concentration. The ratio of $\sigma_{\text{reduced}}/\sigma_{\text{oxidized}}$ of the composite is ~5, supporting its enhanced electrical response as a sensor.

Based on the combination of many considerations, including the designed process based on the phase diagram, comparison of the SEM/EDX and XPS, and detailed analysis of the XRD results, there is no other detectable phase other than Mn_3O_4. This suggests that our designed preparation method was successful at least to the degree that the detection limit of the XPS, EDX and XRD allows us to confirm.

The χ in emu·g^{-1}·Oe^{-1} in the temperature range of 5–350 K under an external magnetic field (H) of 1000 Oe are plotted in Fig. 11. From the data for the $Mn_3O_4/MgFe_2O_4$ composite, the coexistence of the two ferrimagnetic fractions with a larger emphasis on Mn_3O_4 at $T < 42$ K is recognizable. It is worth noting that Mn_3O_4 is ferrimagnetic at low temperatures based on non-collinear arrangement of moments, and has the paramagnetic Curie–Weiss-like behavior at $T > 42$ K [64]. Hence, the dominant effect of ferromagnetic $MgFe_2O_4$ matrix with a ~94% volume fraction is retained in the $Mn_3O_4/MgFe_2O_4$ composite at $T > 42$ K. The M (magnetization)–H (field strength) measurements of the bare $MgFe_2O_4$ and the $Mn_3O_4/MgFe_2O_4$ composite at 5 and 300 K (Fig. 12) show the enhanced magnetization (M_s) of the composite. This observation is different from the observation in a recently reported $MgFe_2O_4/Mn_3O_4$ composite with Mn_3O_4 paramagnetic phase as the main matrix [13].

The H_c (Coercivity) values of bare $MgFe_2O_4$ and $Mn_3O_4/MgFe_2O_4$ composite are in the ranges of 6–7 and 18–20 Oe, respectively, at 300 K. In addition, the magnetic susceptibility decreases with the increasing temperature, showing the same pattern as in many ferrimagnetic materials show [65,66]. Stronger magnetization at lower temperatures is attributed to the frustration effect of the nearest neighbor coupling [67].

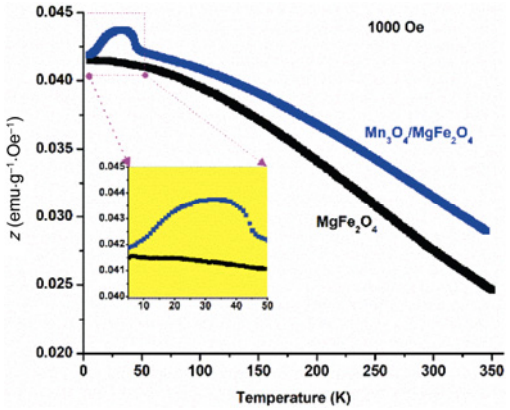

Fig. 11 χ of bare $MgFe_2O_4$ and $Mn_3O_4/MgFe_2O_4$ composite at external field of 1000 Oe.

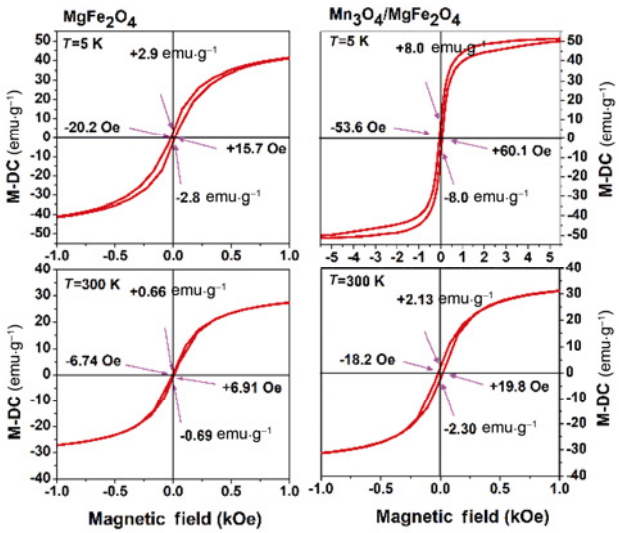

Fig. 12 *M–H* curve of bare $MgFe_2O_4$ and $Mn_3O_4/MgFe_2O_4$ composite at 5 and 300 K.

The magnetic properties also change based on the small structural changes that we observed. $MgFe_2O_4$ shows a ferrimagnetic behavior with antiparallel arrangement of spins of iron at the octahedral [Fe] and tetrahedral (Fe) sites. Increasing the $[Fe^{2+}]/[Fe^{3+}]$ ratio decreases the magnetization due to the lower number of unpaired electrons of Fe^{2+}, and thus its smaller magnetic moment. The experimental magnetic moment ($\boldsymbol{M}_S^{exp.}$, Eq. (S10) in the ESM) of $(Mg_{0.17}Fe^{3+}_{0.83})[Mg_{0.83}Fe^{3+}_{0.39}Fe^{2+}_{0.78}]O_{4-x}$ is equal to $1.32\mu_B$ at 300 K (where μ_B is the Bohr magneton), which is in good agreement with our calculated magnetic moment (Eq. (S11) in the ESM), based on the calculated magnetization ($\boldsymbol{M}_S^{cal.} = 0.39\boldsymbol{\mu}_{[Fe^{3+}]} + 0.78\boldsymbol{\mu}_{[Fe^{2+}]} - 22120.83\boldsymbol{\mu}_{(Fe^{3+})} = 1.22\mu_B$, where $\boldsymbol{\mu}$ is the magnetic moment with the values of $4.9\mu_B$ and $5.9\mu_B$ for Fe^{2+} and Fe^{3+}, respectively, based on their electron spin magnetic moments [67,68]. There is also good agreement between the experimental and theoretical values of magnetic moment for the reduced bare $MgFe_2O_4$, which are $0.69\mu_B$ and $0.83\mu_B$ respectively. This confirms the inversion degree obtained from the XRD pattern and iron valance obtained by the XPS. At $T > 42$ K, the enhanced magnetization is based on the effective role of Mn_3O_4 introduction on the iron oxidation state. Regardless of the similarity in magnetic saturation, there is a considerable difference in the maximum magnetic susceptibility (χ_{max}) of $MgFe_2O_4$ and $Mn_3O_4/MgFe_2O_4$ at weak external magnetic fields (< 110 Oe) (Fig. S5 in the ESM), as summarized in Table 4, reflecting the lower oxidation state of iron under strong oxygen–iron interaction condition and higher oxidation state of iron under poor oxygen–iron interaction condition. This affects the charge transport through the spinel structure discussed by electrical properties under a controlled atmosphere.

Although developing applications such as sensors based on the $Mn_3O_4/MgFe_2O_4$ composite and replacing non-active Mg^{2+} with active transition metal cations such as Zn^{2+} are our future planned studies, one application is demonstrated in Section 4.

4 Chemical sensing application

To test the sensing application of the material, as another example to demonstrate that our instrument can probe the surface reactivity *in situ*, we evaluated the electrical response of the composite to ozone (O_3). 3400 ppm ozone was purged over the $Mn_3O_4/MgFe_2O_4$ composite using the nitrogen gas as the carrier at 150 ℃ (Fig. 13). The ozone purging setup is illustrated in Fig. S10 in the ESM. The fresh composite shows ~200% response ($\Delta R/R_0$, where ΔR is the change to the

Table 4 M_s and χ_{max} of bare $MgFe_2O_4$ and Mn_3O_4-introduced composite

Sample	M_s (emu·g^{-1}), 4 kOe		χ_{max} (emu·g^{-1}·Oe^{-1})		H (Oe)		$\boldsymbol{M}_S^{exp.}$ (μ_B)	$\boldsymbol{M}_S^{cal.}$ (μ_B)
	5 K	300 K	5 K	300 K	5 K	300 K		
$MgFe_2O_4$	53	37	0.197	0.104	75	107	1.32	1.22
$Mn_3O_4/MgFe_2O_4$	54	37	0.254	0.146	63	77	1.34	1.34

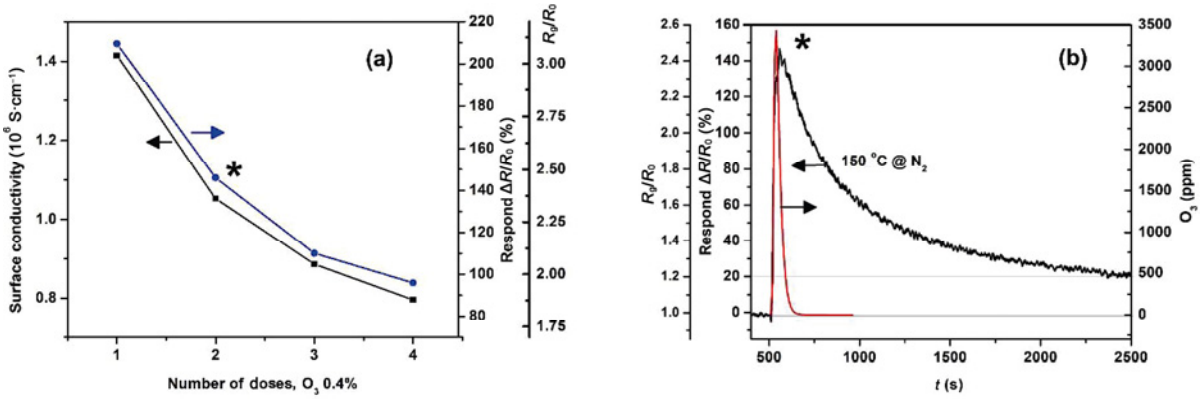

Fig. 13 (a) Changes in electrical response of $Mn_3O_4/MgFe_2O_4$ composite to ozone exposure by 4 sequences of 3400 ppm ozone purged by nitrogen as carrier gas with the flow of 150 mL/min at 150 ℃; (b) ozone concentration of cell vs. time by each ozone purging and one example of electrical response of $Mn_3O_4/MgFe_2O_4$ composite to ozone exposure. R_g is the resistance when the material sis exposed to the gas.

electrical resistance, and R_0 is the electrical resistance before the ozone exposure). By repeating the ozone purging up to 4 times, both the resistance and the electrical response are reduced exponentially as the composite is getting oxidized and saturated by ozone. This saturation is reversible and upon reduction, the resistivity returns to the original value. Increasing the electrical resistance of the material by exposure to ozone confirms the n-type behavior of the composite. Such fast response with considerable change in the oelectrical resistance was not observed for bare $MgFe_2O_4$ and bare Mn_3O_4.

5 Conclusions

Our results are suggestive of the complete reduction of $[Fe^{3+}]$ to $[Fe^{2+}]$, which causes an increase in the E_a of the electron transport at higher temperatures. Most probably, as the temperature increases, there is more electron exchange interaction, which leads to Fe^{2+}-rich octahedral sites, increasing the hopping length. By introducing the intraparticle pores of the Mn_3O_4 phase in the matrix of $MgFe_2O_4$, the synergetic effects of the enhanced mass and charge transport remove the localized structural distortion, and hence decreases the iron involvement in the redox process to keep the average oxidation state of iron high. This leads to the removal of variable-range electron hopping activation.

In conclusion, we show that using a smart compositing method, we can control the position of O in $MgFe_2O_4$ spinels, which in turn affects the distribution of oxidation states among the metal ions in the spinel. Such modification affects the electrical and magnetic properties of the spinel. In addition, in this study, we developed a method to tune the nanocrystalline structure along with the advanced method to tune the electron transport; it would allow us to tune the catalytic properties of the $MgFe_2O_4$. The tunability of our process allowed us to provide a deep understanding of the correlation among many properties, like electron transport and magnetic, catalytic, and sensing properties of the novel semiconductor structures developed by our process.

Author contributions

Khashayar Ghandi has been the principle investigator (PI) and supervised the studies. Farshad Farshidfar and Khashayar Ghandi have initiated the project. Farshad Farshidfar and Arash Fattahi conducted the syntheses. Farshad Farshidfar has done all the conductivity measurements after making the setup. Ralf Brüning has supervised the XRD measurements. Farshad Farshidfar has done all the data analysis other than the analysis of the Mössbauer data taken and analyzed by Dominic H. Ryan. Discussion and revision were first done under supervision of Khashayar Ghandi, and the first draft of the paper was produced by Farshad Farshidfar. The analysis was changed again based on discussions of all coauthors. All coauthors have significantly taken part in the discussions, helped with editing, did the formatting, and helped with the revisions. Most revisions were instructed or done by Khashayar Ghandi and Ralf Brüning.

Data availability statement

Relevant data are available from the corresponding author on request.

Funding

This research was funded by Natural Sciences and Engineering Research Council of Canada to Khashayar Ghandi.

Acknowledgements

The authors thank the Electrochemical Technology Center at University of Guelph for the help with the XPS data collection and Natural Sciences and Engineering Research Council of Canada for funding this work. The authors are also thankful to Ahmed Abdeldaym from Mount Allison University for the XRD measurements and Michel Johnson from Dalhousie University for conducting the magnetic measurements. The authors dedicate this article to all university students in Iran that have been killed only for pursuing human rights in Iran and the world, to all university students in Iran that have been imprisoned or expelled from universities, to all the young people and women in Iran that have been risking their lives and are being killed, injured, tortured, imprisoned, or being raped in prisons, and on almost daily basis for such human rights quests and to women, life, and freedom in Iran.

Declaration of competing interest

The authors have no competing interests to declare that are relevant to the content of this article.

Electronic Supplementary Material

Supplementary material is available in the online version of this article at https://doi.org/10.26599/JAC.2023.9220775.

References

[1] Binns RA, Davis RJ, Reed SJB. Ringwoodite, natural $(Mg,Fe)_2SiO_4$ spinel in the Tenham meteorite. *Nature* 1969, **221**: 943–944.

[2] Mattioli GS, Wood BJ. Upper mantle oxygen fugacity recorded by spinel lherzolites. *Nature* 1986, **322**: 626–628.

[3] McMillan PF. New materials from high-pressure experiments. *Nat Mater* 2002, **1**: 19–25.

[4] Hägg G. The spinels and the cubic sodium–tungsten bronzes as new examples of structures with vacant lattice points. *Nature* 1935, **135**: 874.

[5] Zhou Y, Sun SN, Song JJ, *et al*. Enlarged Co–O covalency in octahedral sites leading to highly efficient spinel oxides for oxygen evolution reaction. *Adv Mater* 2018, **30**: 1802912.

[6] Xiong Y, Xie HY, Rao ZG, *et al*. Compositional modulation in $ZnGa_2O_4$ via Zn^{2+}/Ge^{4+} co-doping to simultaneously lower sintering temperature and improve microwave dielectric properties. *J Adv Ceram* 2021, **10**: 1360–1370.

[7] Swab JJ, Lasalvia JC, Gilde GA, *et al*. Transparent armor ceramics: AlON and spinel. In: *23rd Annual Conference on Composites, Advanced Ceramics, Materials, and Structures: B: Ceramic Engineering and Science Proceedings*. Ustundag E, Fischman G, Eds. Hoboken, USA: John Wiley and Sons, 1999: 79–84.

[8] Belal Hossen M, Akther Hossain AKM. Complex impedance and electric modulus studies of magnetic ceramic $Ni_{0.27}Cu_{0.10}Zn_{0.63}Fe_2O_4$. *J Adv Ceram* 2015, **4**: 217–225.

[9] Ikesue A, Aung YL. Anisotropic alumina ceramics with isotropic optical properties. *J Adv Ceram* 2023, **12**: 72–81.

[10] Joulaei M, Hedayati K, Ghanbari D. Investigation of magnetic, mechanical and flame retardant properties of polymeric nanocomposites: Green synthesis of $MgFe_2O_4$ by lime and orange extracts. *Compos Part B-Eng* 2019, **176**: 107345.

[11] Kharat PB, Somvanshi SB, Khirade PP, *et al*. Induction heating analysis of surface-functionalized nanoscale $CoFe_2O_4$ for magnetic fluid hyperthermia toward noninvasive cancer treatment. *ACS Omega* 2020, **5**: 23378–23384.

[12] Kharat PB, Somvanshi SB, Jadhav KM. Multifunctional magnetic nano-platforms for advanced biomedical applications: A brief review. *J Phys Conf Ser* 2020, **1644**: 012036.

[13] Kaur H, Kaur M, Aggarwal R, *et al*. Nanocomposite of $MgFe_2O_4$ and Mn_3O_4 as polyphenol oxidase mimic for sensing of polyphenols. *Biosensors* 2022, **12**: 428.

[14] Somvanshi SB, Kharat PB, Jadhav KM. Surface functionalized superparamagnetic Zn–Mg ferrite nanoparticles for magnetic hyperthermia application towards noninvasive cancer treatment. *Macromol Symp* 2021, **400**: 2100124.

[15] Somvanshi SB, Thorat ND. Nanoplatforms for cancer imagining. In: *Advances in Image-Guided Cancer Nanomedicine*. Thorat ND, Ed. London, UK: IOP Publishing, 2022: 3-1–3-62.

[16] Tatarchuk T, Bououdina M, Judith Vijaya J, *et al*. Spinel ferrite nanoparticles: Synthesis, crystal structure, properties, and perspective applications. In: *International Conference on Nanotechnology and Nanomaterials—NANO 2016: Nanophysics, Nanomaterials, Interface Studies, and Applications*. Fesenko O, Yatsenko L, Eds. Cham,

Switzerland: Springer Cham, 2017: 305–325.
[17] Hoque SM, Hakim MA, Mamun A, *et al*. Study of the bulk magnetic and electrical properties of $MgFe_2O_4$ synthesized by chemical method. *Mater Sci Appl* 2011, **2**: 1564–1571.
[18] Chen RR, Sun YM, Ong SJH, *et al*. Antiferromagnetic inverse spinel oxide $LiCoVO_4$ with spin-polarized channels for water oxidation. *Adv Mater* 2020, **32**: 1907976.
[19] Zhou Y, Sun SN, Xi SB, *et al*. Superexchange effects on oxygen reduction activity of edge-sharing $[Co_xMn_{1-x}O_6]$ octahedra in spinel oxide. *Adv Mater* 2018, **30**: 1705407.
[20] Zhou Y, Sun SN, Wei C, *et al*. Significance of engineering the octahedral units to promote the oxygen evolution reaction of spinel oxides. *Adv Mater* 2019, **31**: 1902509.
[21] Somvanshi SB, Patade SR, Andhare DD, *et al*. Hyperthermic evaluation of oleic acid coated nano-spinel magnesium ferrite: Enhancement via hydrophobic-to-hydrophilic surface transformation. *J Alloys Compd* 2020, **835**: 155422.
[22] Humbe AV, Kounsalye JS, Somvanshi SB, *et al*. Cation distribution, magnetic and hyperfine interaction studies of Ni–Zn spinel ferrites: Role of Jahn Teller ion (Cu^{2+}) substitution. *Mater Adv* 2020, **1**: 880–890.
[23] Ma JB, Zhao B, Xiang HM, *et al*. High-entropy spinel ferrites MFe_2O_4 (M = Mg, Mn, Fe, Co, Ni, Cu, Zn) with tunable electromagnetic properties and strong microwave absorption. *J Adv Ceram* 2022, **11**: 754–768.
[24] Shunmuga Priya R, Chaudhary P, Ranjith Kumar E, *et al*. Evaluation of structural, dielectric and electrical humidity sensor behaviour of $MgFe_2O_4$ ferrite nanoparticles. *Ceram Int* 2021, **47**: 15995–16008.
[25] Guo JH, Shi L, Wu L, *et al*. Spin-polarized electron transport in highly reduced $MgFe_2O_{4-\delta}$. *Mater Res Express* 2018, **5**: 126301.
[26] Benko FA, Koffyberg FP. The effect of defects on some photoelectrochemical properties of semiconducting $MgFe_2O_4$. *Mater Res Bull* 1986, **21**: 1183–1188.
[27] Li JT, Chu D, Dong H, *et al*. Boosted oxygen evolution reactivity by igniting double exchange interaction in spinel oxides. *J Am Chem Soc* 2020, **142**: 50–54.
[28] Yamamoto T, Kageyama H. Hydride reductions of transition metal oxides. *Chem Lett* 2013, **42**: 946–953.
[29] Arandiyan H, Mofarah SS, Sorrell CC, *et al*. Defect engineering of oxide perovskites for catalysis and energy storage: Synthesis of chemistry and materials science. *Chem Soc Rev* 2021, **50**: 10116–10211.
[30] Sugiyama J, Atsumi T, Hioki T, *et al*. Oxygen nonstoichiometry of spinel $LiMn_2O_{4-\delta}$. *J Alloys Compd* 1996, **235**: 163–169.
[31] Cao L, Petracic O, Zakalek P, *et al*. Reversible control of physical properties via an oxygen-vacancy-driven topotactic transition in epitaxial $La_{0.7}Sr_{0.3}MnO_{3-\delta}$ thin films. *Adv Mater* 2019, **31**: 1806183.
[32] Kovtunenko PV. Defect formation in spinels in oxygen nonstoichiometry (a review). *Glass Ceram* 1997, **54**: 143–148.
[33] Shao ZY, Zhu Q, Sun Y, *et al*. Phase-reconfiguration-induced $NiS/NiFe_2O_4$ composite for performance-enhanced zinc–air batteries. *Adv Mater* 2022, **34**: 2110172.
[34] Kalaiselvan CR, Laha SS, Somvanshi SB, *et al*. Manganese ferrite ($MnFe_2O_4$) nanostructures for cancer theranostics. *Coord Chem Rev* 2022, **473**: 214809.
[35] Wang MS, Sundman B. Thermodynamic assessment of the Mn–O system. *Metall Trans B* 1992, **23**: 821–831.
[36] Kang YB, Jung IH. Thermodynamic modeling of oxide phases in the Mn–O system. *Metall Mater Trans E* 2016, **3**: 156–170.
[37] Terayama K, Ikeda M. Study on thermal decomposition of MnO_2 and Mn_2O_3 by thermal analysis. *Trans JIM* 1983, **24**: 754–758.
[38] Mustapha S, Ndamitso MM, Abdulkareem AS, *et al*. Comparative study of crystallite size using Williamson–Hall and Debye–Scherrer plots for ZnO nanoparticles. *Adv Nat Sci Nanosci Nanotechnol* 2019, **10**: 045013.
[39] Kim KS, Muralidharan P, Han SH, *et al*. Influence of oxygen partial pressure on the epitaxial $MgFe_2O_4$ thin films deposited on $SrTiO_3$ (100) substrate. *J Alloys Compd* 2010, **503**: 460–463.
[40] Somvanshi SB, Khedkar MV, Kharat PB, *et al*. Influential diamagnetic magnesium (Mg^{2+}) ion substitution in nano-spinel zinc ferrite ($ZnFe_2O_4$): Thermal, structural, spectral, optical and physisorption analysis. *Ceram Int* 2020, **46**: 8640–8650.
[41] Somvanshi SB, Jadhav SA, Khedkar MV, *et al*. Structural, thermal, spectral, optical and surface analysis of rare earth metal ion (Gd^{3+}) doped mixed Zn–Mg nano-spinel ferrites. *Ceram Int* 2020, **46**: 13170–13179.
[42] O'neill HSC, Annersten H, Virgo D. The temperature dependence of the cation distribution in magnesioferrite ($MgFe_2O_4$) from powder XRD structural refinements and Mössbauer spectroscopy. *Am Mineral* 1992, **77**: 725–740.
[43] Gateshki M, V Petkov, Pradhan SK, *et al*. Structure of nanocrystalline $MgFe_2O_4$ from X-ray diffraction, Rietveld and atomic pair distribution function analysis. *J Appl Cryst* 2005, **38**: 772–779.
[44] Bertaut EF. Sur quelques progrès récents dans la cristallographie des spinelles, en particulier des ferrites. *J Phys Radium* 1951, **12**: 252–255. (in French)
[45] Sickafus KE, Wills JM, Grimes NW. Structure of spinel. *J Am Ceram Soc* 1999, **82**: 3279–3292.
[46] Antao SM, Hassan I, Parise JB. Cation ordering in magnesioferrite, $MgFe_2O_4$, to 982 ℃ using *in situ* synchrotron X-ray powder diffraction. *Am Mineral* 2005, **90**: 219–228.
[47] Shaikh AM, Jadhav SA, Watawe SC, *et al*. Infrared spectral studies of Zn-substituted Li–Mg ferrites. *Mater Lett* 2000, **44**: 192–196.
[48] Sawant SR, Suryavanshi SS. Iono-covalent and Yafet Kittle (YK) angle studies of slow cooled and quenched CuZn-system. *Curr Sci* 1988, **57**: 644–647.
[49] Nagarajan V, Thayumanavan A, Chandiramouli R.

Magnesium ferrite nanostructures for detection of ethanol vapours—A first-principles study. *Process Appl Ceram* 2017, **11**: 296–303.

[50] Sekulić DL, Lazarević ZZ, Jovalekić CD, *et al*. Impedance spectroscopy of nanocrystalline $MgFe_2O_4$ and $MnFe_2O_4$ ferrite ceramics: Effect of grain boundaries on the electrical properties. *Sci Sinter* 2016, **48**: 17–28.

[51] Sawatzky GA, Coey JMD, Morrish AH. Mössbauer study of electron hopping in the octahedral sites of Fe_3O_4. *J Appl Phys* 1969, **40**: 1402–1403.

[52] Skomurski FN, Kerisit S, Rosso KM. Structure, charge distribution, and electron hopping dynamics in magnetite (Fe_3O_4) (100) surfaces from first principles. *Geochim Cosmochim Ac* 2010, **74**: 4234–4248.

[53] Morris ER, Williams Q. Electrical resistivity of Fe_3O_4 to 48 GPa: Compression-induced changes in electron hopping at mantle pressures. *J Geophys Res-Sol Ea* 1997, **102**: 18139–18148.

[54] Nell J, Wood BJ. High-temperature electrical measurements and thermodynamic properties of Fe_3O_4–$FeCr_2O_4$–$MgCr_2O_4$–$FeAl_2O_4$ spinels. *Am Mineral* 1991, **76**: 405–426.

[55] Ling H, Petric A. Electrical and thermal properties of spinels. *Proc Vol* 2005, **2005–2007**: 1866–1873.

[56] Dhaouadi H, Madani A, Touati F. Synthesis and spectroscopic investigations of Mn_3O_4 nanoparticles. *Mater Lett* 2010, **64**: 2395–2398.

[57] Dhaouadi H, Ghodbane O, Hosni F, *et al*. Mn_3O_4 nanoparticles: Synthesis, characterization, and dielectric properties. *ISRN Spectrosc* 2012, **2012**: 706398.

[58] Larson EG, Arnott RJ, Wickham DG. Preparation, semiconduction and low-temperature magnetization of the system $Ni_{1-x}Mn_{12+x}O_4$. *J Phys Chem Solids* 1962, **23**: 1771–1781.

[59] Bhosale AB, Somvanshi SB, Murumkar VD, *et al*. Influential incorporation of RE metal ion (Dy^{3+}) in yttrium iron garnet (YIG) nanoparticles: Magnetic, electrical and dielectric behaviour. *Ceram Int* 2020, **46**: 15372–15378.

[60] Verwey EJ, Haayman PW, Romeijn FC. Physical properties and cation arrangement of oxides with spinel structures II. electronic conductivity. *J Chem Phys* 1947, **15**: 181–187.

[61] Bloesser A, Kurz H, Timm J, *et al*. Tailoring the size, inversion parameter, and absorption of phase-pure magnetic $MgFe_2O_4$ nanoparticles for photocatalytic degradations. *ACS Appl Nano Mater* 2020, **3**: 11587–11599.

[62] Podwórny J. XRD based methods of investigation the order–disorder transformation in the spinel structure—A comparative study. *Solid State Phenom* 2013, **203–204**: 129–132.

[63] Cao W, Tan OK, Pan JS, *et al*. XPS characterization of xα-Fe_2O_3–$(1-x)ZrO_2$ for oxygen gas sensing application. *Mater Chem Phys* 2002, **75**: 67–70.

[64] Ghigna P, de Renzi R, Mozzati MC, *et al*. Magnetism of $Mg_{1-x}Mn_xO_4$ spinels by SQUID magnetometry and muon spin rotation spectroscopy. *Phys Rev B* 2006, **73**: 184402.

[65] Sawatzky GA, van Der Woude F, Morrish AH. Mössbauer study of several ferrimagnetic spinels. *Phys Rev* 1969, **187**: 747–757.

[66] Zhang C, Lv ZL, Wu JK, *et al*. Enhanced ferroelectric and ferrimagnetism properties at room temperature in $BaTiO_3$ doped $GaFeO_3$ ceramics. *Chem Phys Lett* 2023, **813**: 140316.

[67] Borhan AI, Ghercă D, Iordan AR, *et al*. Classification and types of ferrites. *Ferrite Nanostructured Magnetic Materials: Technologies and Applications*. Pal Singh J, Chae KH, Srivastava RC, *et al*. Eds. Sawston Cambridge, UK: Woodhead Publishing, 2023: 17–34.

[68] Coey JMD. *Magnetism and Magnetic Materials*. Cambridge, UK: Cambridge University Press, 2010.